

# SIMULATION OF ROOM TRANSFER FUNCTIONS WITH DIRECTIVITY PATTERNS ON THE BASIS OF MODES

Franz Zotter<sup>1</sup>, Andrés Ureta Staackmann<sup>2</sup>,

<sup>1</sup>*Institute of Electronic Music and Acoustics, Univ. Music and Performing Arts, 8010 Graz, Austria, Email: zotter@iem.at*

<sup>2</sup>*University of Music and Performing Arts, 8010 Graz, Austria, Email: andres.staackmann@gmail.com*

## Introduction

The simulation of room impulse responses (RIR) for directional sources and receivers in arbitrarily-shaped rooms has been subject of research in numerous publications, e.g. [1, 2, 3]. Simulations nowadays involve numerous successful efforts [4, 5] to achieve auralization.

By contrast, this study aims at simplistic source-and-receiver-directional room impulse response (srdRIR) modeling and therefore considers the case of a perfectly sound-hard rectangular room. By this, we carry on the work of Pollow et al. [6] who extended the room mode method by source and receiver directivity using multipole derivatives. They compared results with the boundary element method. As the simplistic case is solved by the image source method and the room mode method as two co-existing analytic methods [7], we review differences between them using exemplary multipole derivatives and directional analysis of the resulting srdRIR. The main difference between the room mode and image source method are the domain of summation: (i) discrete room modes in case of the room mode method, (ii) discrete image sources in case of the image source method.

**Room mode solution omnidirectional.** The mode solution for an omnidirectional source at  $\mathbf{r}' = [x', y', z']^T$  and an omnidirectional receiver at  $\mathbf{r} = [x, y, z]^T$  in a sound-hard  $L_x \times L_y \times L_z$  rectangular room is [1, 7]

$$H_0 = \boldsymbol{\psi}^T(\mathbf{r}) \text{diag}\{\mathbf{b}(\omega)\} \boldsymbol{\psi}(\mathbf{r}'). \quad (1)$$

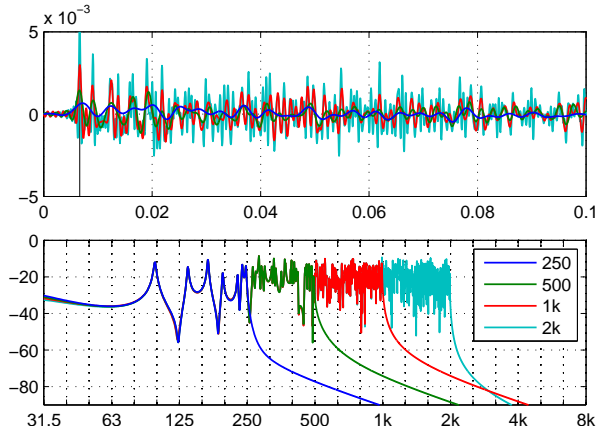
The vector  $\mathbf{b}(\omega) = [b_{uvw}(\omega)]$  contains modal resonances  $b_{uvw}(\omega) = \frac{c^2(2\pi)^{-1}}{\omega_{uvw}^2 - (\omega - i\sigma)^2}$  for non-negative indices  $(u, v, w)$  ringing at the frequencies  $\omega_{uvw} = \pi c \sqrt{\frac{u^2}{L_x^2} + \frac{v^2}{L_y^2} + \frac{w^2}{L_z^2}}$ ;  $\sigma = 3 \ln(10)/T_{60}$  yields a finite reverberation time. The vector  $\boldsymbol{\psi} = [\psi_{uvw}(\mathbf{r})]$  contains the respective room modes  $\psi_{uvw} = N_u N_v N_w \cos(\frac{\pi}{L_x} u x) \cos(\frac{\pi}{L_y} v y) \cos(\frac{\pi}{L_z} w z)$  normalized by  $N_u^2 = (2 - \delta_u)/L_x$ ,  $N_v^2 = (2 - \delta_v)/L_y$ ,  $N_w^2 = (2 - \delta_w)/L_z$ . Typically, the vectors contain a finite set of modes below an upper frequency limit  $\omega_{uvw} \leq \omega_{\max}$ .

**Image source solution omnidirectional.** Here Green's function  $G = e^{-ik\|\mathbf{r}-\mathbf{r}'\|} (4\pi\|\mathbf{r}-\mathbf{r}'\|)^{-1}$  is displaced and mirrored periodically in space yielding [1, 7]

$$H_0 = \sum_{u=-\infty}^{\infty} \sum_{v=-\infty}^{\infty} \sum_{w=-\infty}^{\infty} G \left( \begin{array}{l} x - [u L_x + (-1)^u x'] \\ y - [v L_y + (-1)^v y'] \\ z - [w L_z + (-1)^w z'] \end{array} \right). \quad (2)$$

By limiting the time-delay  $\tau_{uvw} = \|\mathbf{r} - \mathbf{r}'_{uvw}\|/c \leq \tau_{\max}$ , we obtain a finite sum.

**Figure 1:** Impulse and frequency response of the room mode method (omnidirectional) for several modal cutoff frequencies; the highpass filter  $(if/10)^2/(1+if/10)^2$  and  $T_{60} = 1s$  was used to stabilize the shape of the impulse response. Room is  $7 \times 5 \times 3m$ , source at  $(3.5, 2.5, 3.5)$ , receiver at  $(1.75, 1.25, 0.75)$ .



## Multipole derivative operator

An operator of the form, cf. [6, 8],

$$\partial_{xyz}^{lmn} := (-ik)^{-(l+m+n)} \frac{\partial^l}{\partial x^l} \frac{\partial^m}{\partial y^m} \frac{\partial^n}{\partial z^n} \quad (3)$$

can be applied to  $H_0$  to describe directivity at source and receiver, or to the free-field Green's function  $G = (4\pi r)^{-1} e^{-ikr}$ , which originally only depends on the distance  $r$ . Far away,  $\partial_{xyz}^{lmn} G$  becomes (see appendix I)

$$\lim_{r \rightarrow \infty} \partial_{xyz}^{lmn} G = \theta_x^l \theta_y^m \theta_z^n G = M_{lmn}(\boldsymbol{\theta}) G, \quad (4)$$

with  $\boldsymbol{\theta} = \mathbf{r}/r$  representing the direction  $\boldsymbol{\theta}^T = [\theta_x, \theta_y, \theta_z] = [\cos \varphi \sin \vartheta, \sin \varphi \sin \vartheta, \cos \vartheta]$  from which the source is received. Moreover, the *multipole* directivities  $M_{lmn}(\boldsymbol{\theta})$  depend on indices specifying the number of derivatives with regard to each coordinate.

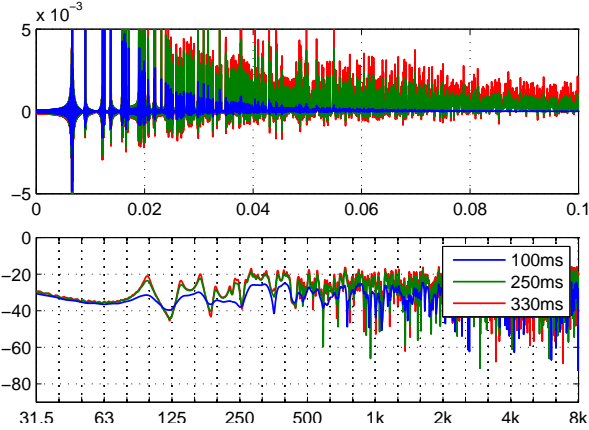
Any  $N^{\text{th}}$ -order directivity can be decomposed into the basis of  $(N+1)(N+2)(N+3)/3$  *multipoles* of the  $N^{\text{th}}$  order. We specify far-field directivities of source and receiver by

$$g(\boldsymbol{\theta}) = \sum_{l=0}^N \sum_{m=0}^{N-l} \sum_{n=0}^{N-l-m} \gamma_{lmn} M_{lmn}(\boldsymbol{\theta}) = \boldsymbol{m}^T(\boldsymbol{\theta}) \boldsymbol{\gamma}, \quad (5)$$

in terms of the multipole expansion coefficients  $\gamma_{lmn}$ . They determine the response for particular directivities  $\gamma_{lmn}^{(R)}$ ,  $\gamma_{l'm'n'}^{(S)}$  as the linear combination of multipole-to-multipole responses  $H_{lmn}^{l'm'n'} := \partial_{xyz}^{lmn} \partial_{x'y'z'}^{l'm'n'} H_0$ ,

$$H = \sum_{lmn} \sum_{l'm'n'} \gamma_{lmn}^{(R)} H_{lmn}^{l'm'n'} \gamma_{l'm'n'}^{(S)}. \quad (6)$$

**Figure 2:** Impulse and frequency response of the room mode method (omnidirectional) for several time limits  $\tau_{\max}$ ; the envelope  $10^{-60 \frac{t}{20\tau_{\max}}}$  stabilizes temporal shape and response spectrum (room geometry as before).



### Application to the room mode method

For a mode index  $u$  and coordinate  $x$ , structurally for every factor of the spatial modes resembling  $\cos(\frac{\pi}{L}ux)$ ,  $l$ -fold differentiation wrt. source or receiver coordinates yields manipulation to, cf. [8],

$$\frac{d^l \cos(\frac{\pi}{L}ux)}{dx^l} = (\frac{\pi}{L}u)^l [\cos(\frac{\pi}{L}ux) \cos(\frac{\pi}{2}l) - \sin(\frac{\pi}{L}ux) \sin(\frac{\pi}{2}l)].$$

Then  $\partial_{xyz}^{lmn} \partial_{x'y'z'}^{l'm'n'} H_0$  contains modes accordingly modified

$$H_{lmm'n'}^{l'm'n'} = (-ik)^{-a} \psi_{lmm}^T(\mathbf{r}) \text{diag}\{\mathbf{b}(\omega)\} \psi_{l'm'n'}(\mathbf{r}')$$

to their multipole derivatives;  $a = l + l' + n + n' + m + m'$ .

### Application to the image source method

For any coordinate, Green's functions in the image source method depend on image index  $u$ , receiver coordinate  $x$ , and source coordinate  $x'$ ,  $G = G(x + (-1)^{u+1}x' - uL_x)$ . Derivatives wrt.  $x'$  and  $x$  are related by a sign change  $\frac{\partial}{\partial x'} = (-1)^{u+1} \frac{\partial}{\partial x}$ . Both  $l$ -fold receiver-coordinate and  $l'$ -fold source-coordinate differentiation for  $\partial_{xyz}^{lmn} \partial_{x'y'z'}^{l'm'n'} H_0$  can be aggregated for the image source index  $u$  along  $x$  to  $\frac{\partial^l}{\partial x^l} \frac{\partial^{l'}}{\partial x'^{l'}} = (-1)^{l'(u+1)} \frac{\partial^{l+l'}}{\partial x^{l+l'}}$ , and in the same way for the other coordinates. The far-field approximation Eq. (4) performs reasonably well for the directivities, and it offers simple and fast calculation, cf. Fig. 3 and appendix II.

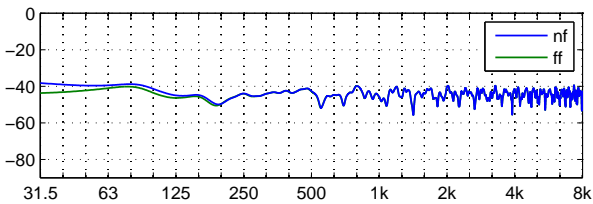


**Figure 3:** Frequency response  $H_{010}^{100} = \partial_{xyz}^{010} \partial_{x'y'z'}^{100} H_0$  of the image source method for  $\tau_{\max} = 50$  ms as accurate solution (nf) and far-field approximation (ff); in addition to envelope  $10^{-60 \frac{t}{20\tau_{\max}}}$ , nf was stabilized by  $(if/15)^a / (1 + if/15)^a$ ,  $a = 2 \dots$  total number of derivatives (room geometry as before).

## Comparison of resulting $H_0$ , $H_{000}^{100}$ , $H_{010}^{100}$

The room mode method produces stable results after regularization of the 0 Hz mode by a second-order highpass, cf. Figs. 1, 4(a), 4(c). Here, synthesis was done in the discrete Fourier domain, so damping  $T_{60} < \infty$  was applied to avoid cyclic inverse Fourier transform. The result exhibits sharp spectral peaks at resonance frequencies and steeply decays above the summation limit  $f_{\max}$ . Accordingly, sinc-shaped impulses in the temporal response resemble the characteristics of a zero-phase lowpass. Concerning multipole-derived responses in Fig. 4(c), the room mode method is less robust and requires additional low-frequency stabilization. This is caused by the weak spectral decay  $\lim_{\omega \rightarrow 0} \frac{1}{\omega^2 - \omega_u^2} = \frac{1}{\omega_u^2}$  of high-frequency modes, which is counter-acted by the  $l$ -fold differentiation amplifying these modes by  $\omega_u^l$ . What is more, the modal density around the mode  $u$  is proportional to  $\omega_u^2$ , therefore the rather stochastic factor  $\psi_u(x)\psi_u(x')$  is not always enough to ensure numerical stability at low frequencies.

To avoid spectral ripple for the image source model, and to facilitate comparison, an exponential window  $10^{-60 \frac{t}{20\tau_{\max}}}$  was imposed on the resulting impulse response, see Figs. 2, 4(b), 4(d). Due to the synthesis in the frequency domain, the image source method exhibits sinc-shaped fractional delays in the time domain. Still, temporal peaks are sharp. In case of the accurate solution in appendix II, the order of the DC-stabilizing highpass must increase with the derivative order.

Despite the resulting spectral and temporal similarities, the image source method does not provide full-length simulation of impulse responses, while the room mode method does not provide their full-spectrum simulation.

## Directional analysis

### Spherical harmonics instead of multipoles

The spherical harmonics only use  $(N+1)^2$  terms to decompose an  $N^{\text{th}}$ -order directivities alternatively to Eq. (5)

$$g(\boldsymbol{\theta}) = \sum_{n=0}^N \sum_{m=-n}^n Y_n^m(\boldsymbol{\theta}) \gamma_{nm}^{(\text{SH})} = \mathbf{y}^T(\boldsymbol{\theta}) \boldsymbol{\gamma}^{(\text{SH})} \quad (7)$$

using spherical harmonics up to order  $N$

$$Y_n^m(\boldsymbol{\theta}) = \sqrt{\frac{(2n+1)(n-|m|)!}{2(n+|m|)!}} P_n^m(\theta_z) \Phi_m(\varphi), \quad (8)$$

$$\Phi_m(\varphi) = \sqrt{\frac{(2-\delta_m)}{2\pi}} \begin{cases} \sin(|m|\varphi), & m < 0 \\ \cos(|m|\varphi), & m \geq 0, \end{cases} \quad (9)$$

where  $P_n^m(\cdot)$  are associated Legendre / Ferrer's functions. To convert between expansion coefficients  $\boldsymbol{\gamma}^{(\text{SH})}$  and  $\boldsymbol{\gamma}$ , we equate the expansions of  $g(\boldsymbol{\theta})$  evaluated at all nodes of a  $t = 2N$ -design sampling grid,  $\mathbf{g} = [g(\boldsymbol{\theta}_1), \dots, g(\boldsymbol{\theta}_L)]^T$ ,

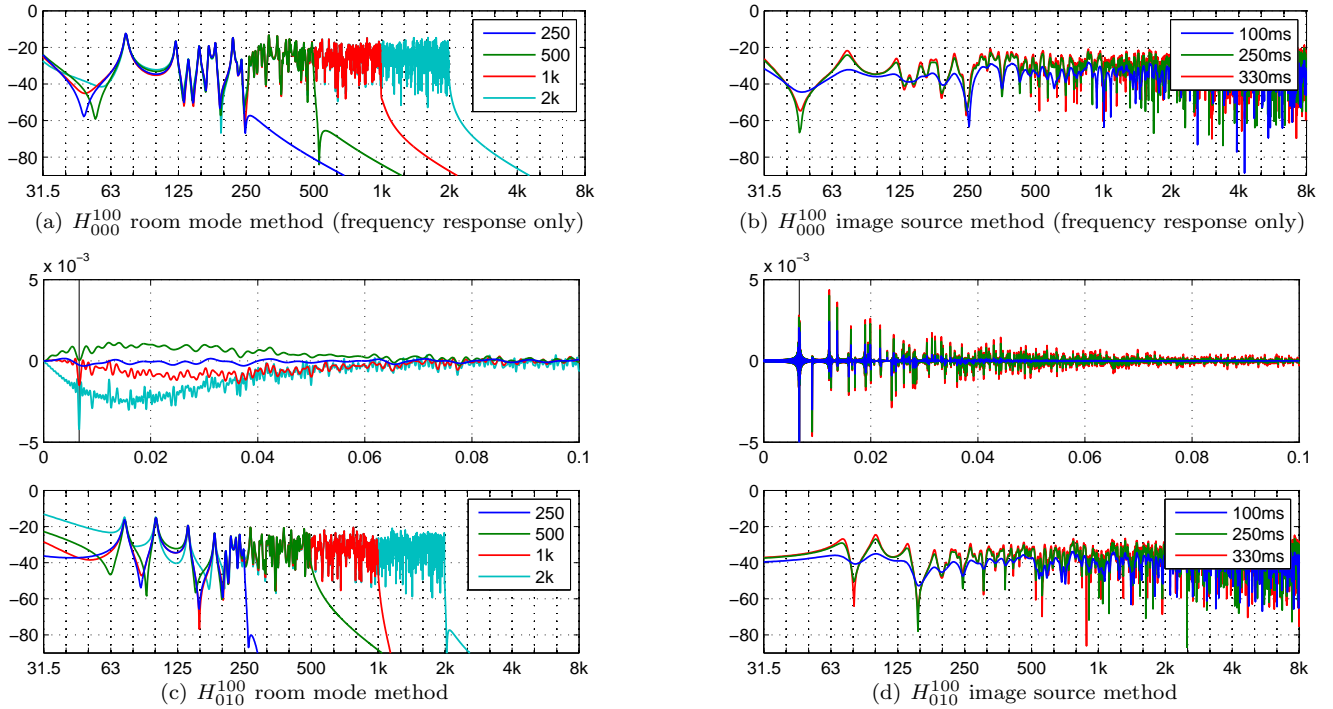
$$\mathbf{g} = \mathbf{Y} \boldsymbol{\gamma}^{(\text{SH})} = \mathbf{M} \boldsymbol{\gamma}. \quad (10)$$

With the pseudoinverse denoted as  $(\cdot)^\dagger$ , we obtain

$$\boldsymbol{\gamma} = \mathbf{M}^\dagger \mathbf{Y} \boldsymbol{\gamma}^{(\text{SH})} = \mathbf{C} \boldsymbol{\gamma}^{(\text{SH})}. \quad (11)$$

A  $2N$ -design [11] as sampling criterion avoids aliasing and yields well-conditioned  $\mathbf{M}$  and  $\mathbf{Y}$ ; also  $\mathbf{Y}^\dagger = \frac{4\pi}{L} \mathbf{Y}^T$ .

**Figure 4:** Impulse and frequency responses of room mode and image source methods for  $H_{000}^{100} = \partial_{xyz}^{000} \partial_{x'y'z'}^{100} H_0$  and  $H_{010}^{100} = \partial_{xyz}^{010} \partial_{x'y'z'}^{100} H_0$  for several modal/temporal cutoffs; highpass and envelope for room mode method were  $(if/10)^2/(1+if/10)^2$  and  $T_{60} = 1s$ , and for the image source method  $10^{-60 \frac{t}{20\tau_{\max}}}$  (room geometry as before).



### Source-and-receiver-directional RIR (srdRIR)

By  $\mathbf{C}$  in Eq. (11), the linearly combined multipole-to-multipole responses Eq. (6),  $\mathbf{H}_{MP}(t) = [H_{lmn}^{l'm'n'}(t)]$ , is converted to spherical-harmonics-to-spherical-harmonics

$$\begin{aligned} h(t) &= \gamma_{MP(R)}^T \mathbf{H}_{MP}(t) \gamma_{MP(S)} \\ &= \gamma_R^T \mathbf{C}^T \mathbf{H}_{MP}(t) \mathbf{C} \gamma_S = \gamma_R^T \mathbf{H}(t) \gamma_S. \end{aligned} \quad (12)$$

The SH-domain srdRIR  $\mathbf{H}(t)$  expanded in spherical harmonics yields a ray-domain srdRIR, an impulse response of a source that exclusively emits sound towards  $\theta_S$  and a receiver that exclusively picks up sound from  $\theta_R$ ,

$$h(\theta_R, t, \theta_S) = \mathbf{y}(\theta_R)^T \mathbf{H}(t) \mathbf{y}(\theta_S). \quad (13)$$

$h(\theta_R, t, \theta_S)$  peaks at arrival times, provided that the ray directions  $\theta_S, \theta_R$  match the corresponding emitting and receiving directions of the acoustic path, cf. [9].

The orthonormality  $\int_{S^2} \mathbf{y}(\theta) \mathbf{y}(\theta)^T d\theta = \mathbf{I}$  of the spherical harmonics enables deriving the SH-domain RIR Eq.(12) from the ray-domain srdRIR Eq. (13) by integration with the source and receiver directivities Eq. (7)  $g(\theta_S), g(\theta_R)$ ,

$$h(t) = \iint_{S^2} g(\theta_R) h(\theta_R, t, \theta_S) g(\theta_S) d\theta_R d\theta_S. \quad (14)$$

### Ray-domain energy maps

To simplify ray-domain inspection, a map is defined at the receiver accumulated over all emission directions as

$$\begin{aligned} h^2(\theta_R, t) &= \int_{S^2} h^2(\theta_R, t, \theta_S) d\theta_S \\ &= \mathbf{y}(\theta_R)^T \mathbf{H}(t) \mathbf{H}(t)^T \mathbf{y}(\theta_R); \end{aligned} \quad (15)$$

and  $h^2(t, \theta_S) = \mathbf{y}(\theta_S)^T \mathbf{H}(t)^T \mathbf{H}(t) \mathbf{y}(\theta_S)$  at the source.

**Example:** A rectangular room of the dimensions  $4.5 \times 3.1 \times 2.2$  was simulated using both methods. The receiver and source were placed at  $(1.2, 3.1, 2.2)$  and  $(2.5, 0.8, 1)$ , and the srdRIR was simulated up to 2<sup>nd</sup> order. Energy maps for selected arrival times are shown in Tab. 1, cf. [8]. Early reflections are resolved more clearly in energy maps of the image source method. They indicate the emitting and receiving ray directions. While the mapping of the room mode method is just less accurate for direct and 1<sup>st</sup>-order reflected sound (1<sup>st</sup> and 2<sup>nd</sup> line in Tab. 2), its low temporal resolution around the 2<sup>nd</sup>-order reflection causes a mix of adjacent reflections (3<sup>rd</sup> line in Tab. 1).

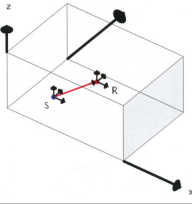
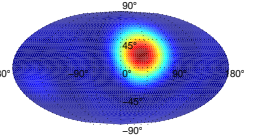
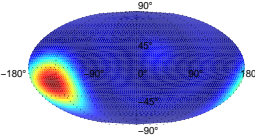
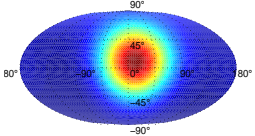
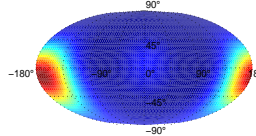
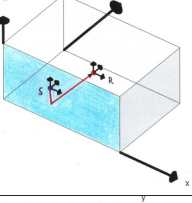
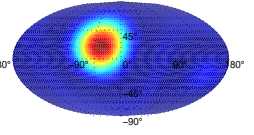
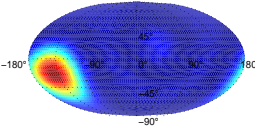
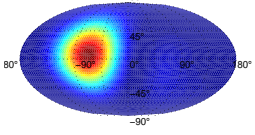
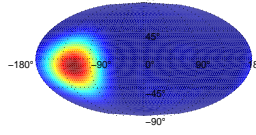
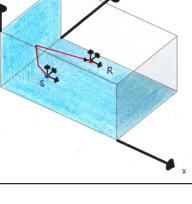
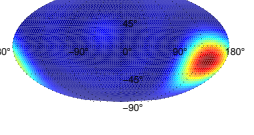
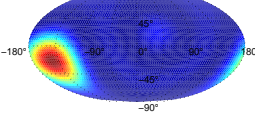
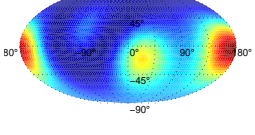
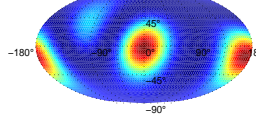
### Conclusions

We compared the room mode method and the image source method to simulate responses of a sound-hard rectangular room. To involve source and receiver directivities, we utilized multiple Cartesian derivatives. While we did not find a far-field approximation for the room mode method, we expect the far-field approximated result of the image source method to typically be accurate enough.

To enable comparison, both methods were stabilized, i.e., by exponential temporal weighting for the image source method and by 2<sup>nd</sup> order high-pass filtering for the room mode method. Impulse responses of the image source method are better resolved but finite in time, while frequency responses of the room mode method are better resolved but finite in the spectrum.

For high-order directivities, the room mode method exhibits convergence problems at low frequencies. Directionally, energy maps indicate smaller accuracy of the room mode method. Moreover because of its inferior temporal resolution, directions of similar flight times tend to mix.

**Table 1:** Energy maps of exemplary acoustic paths for the image source and room mode method.

Path	image source method		room mode method	
	$h^2(t, \theta_S)$	$h^2(\theta_R, t)$	$h^2(t, \theta_S)$	$h^2(\theta_R, t)$
				
				
				

## References

- [1] H. Kuttruff: Room Acoustics. Spon Press (UK), 2000.
- [2] M. Vorländer: Auralization. Springer, 2007.
- [3] L. Savioja, P. Svensson: Overview of geometrical room acoustic modeling techniques. JASA 138(2), 2015.
- [4] A. Wabnitz, N. Epain, C. Jin, A. v. Schaik: Room Acoustics Simulation for multichannel microphone arrays, 2010. <http://sydney.edu.au/engineering/electrical/carlab/mcroomsim.htm>
- [5] M. Noisternig, B.F.G. Katz, S. Siltanen, L. Savioja: Framework for real-time auralization in architectural acoustics. Acta Acustica u. Acustica 94(6), 2008.
- [6] M. Pollow, P. Dietrich, M. Vorländer: Room impulse responses of rectangular rooms for sources and receivers of arbitrary directivity, AIA-DAGA 2013.
- [7] J.B. Allen, D.A. Berkley: Image method for efficiently simulating small-room acoustics. JASA 65(4), 1979.
- [8] A. Ureta Staackmann: Simulation of room transfer functions with directivity patterns on the basis of modes. M. Thesis, Univ. Music and Performing Arts Graz, 2014.
- [9] H. Morgenstern, F. Zotter, B. Rafely: Joint spherical beam forming for directional analysis of reflections in rooms. acoustics-2012, Hong Kong, 2012.
- [10] N.A. Gumerov, R. Duraiswami: Fast multipole methods for the Helmholtz equation in three dimensions. Elsevier, 2005.
- [11] M. Gräf: Efficient algorithms for the computation of optimal quadrature points on Riemannian manifolds. PhD. Thesis, TU Chemnitz, 2013. <http://homepage.univie.ac.at/manuel.graef/quadrature.php>

**Appendix I:** multiple derivatives with  $\frac{\partial}{\partial x} = \frac{x}{r} \frac{\partial}{\partial r}$  become

$$\begin{aligned}
 \lim_{r \rightarrow \infty} \frac{\partial^l}{\partial x^l} G &= \frac{\partial^{l-1}}{\partial x^{l-1}} \lim_{r \rightarrow \infty} \left[ \frac{x}{r} \right] \frac{\partial}{\partial r} G \\
 &= \frac{\partial^{l-2}}{\partial x^{l-2}} \lim_{r \rightarrow \infty} \left[ \frac{r^2 - x^2}{r^3} + \frac{x^2}{r^2} \frac{\partial}{\partial r} \right] \frac{\partial}{\partial r} G \\
 &= \theta_x^l \lim_{r \rightarrow \infty} \frac{\partial^l}{\partial r^l} G = \theta_x^l \frac{\partial^{l-1}}{\partial r^{l-1}} \lim_{r \rightarrow \infty} \left[ -ik - \frac{1}{r} \right] G \\
 &= (-ik)^l \theta_x^l G,
 \end{aligned}$$

**Appendix II:** to avoid far-field approximation, Green's function  $G$  is written as 0<sup>th</sup>-order spherical basis solution

$$G = -\frac{ik}{\sqrt{4\pi}} h_0^{(2)} Y_0^0(-\theta) = -\frac{ik}{\sqrt{4\pi}} \mathbf{b}^T \mathbf{e}_0, \quad (16)$$

with the vector  $\mathbf{b} = [h_n Y_n^m]_{nm}$  containing all basis solutions composed of spherical Hankel functions and spherical harmonics,  $\mathbf{e}_0 = [1, 0, \dots]$ . Cartesian differentials re-expand to spherical basis solutions by sparse, frequency-independent matrices,  $\frac{\partial}{\partial x} \mathbf{b} = \mathbf{D}_x \mathbf{b}$ , cf. [10], so that

$$\frac{\partial^l}{\partial x^l} \frac{\partial^m}{\partial y^m} \frac{\partial^n}{\partial z^n} \mathbf{b} = k^{l+n+m} (\mathbf{D}_x)^l (\mathbf{D}_y)^m (\mathbf{D}_z)^n \mathbf{b}. \quad (17)$$

## Acknowledgment

The presentation of this contribution at DAGA 2017 was enabled by the Austrian Science Fund (FWF) project nr. AR 328-G21, Orchestrating Space by Icosahedral Loudspeaker.